HHS Public Access

Author manuscript

Atmos Environ (1994). Author manuscript; available in PMC 2015 November 09.

Published in final edited form as:

Atmos Environ (1994). 2013 December ; 80: 204–215. doi:10.1016/j.atmosenv.2013.07.057.

Low-wind and other microclimatic factors in near-road black carbon variability: A case study and assessment implications

Marissa S. Liang[a], **Timothy C. Keener**[a,*], **M. Eileen Birch**[b], **Richard Baldauf**[c], **Jill Neal**[d], and **Y. Jeffrey Yang**[d]

[a] University of Cincinnati, Department of Biomedical, Chemical, and Environmental Engineering, College of Engineering and Applied Science, P.O. Box 210012, Cincinnati, OH 45221-0012, USA

[b] U.S. Center for Disease Control, National Institute of Occupational Safety and Health, 5555 Ridge Avenue, Cincinnati, OH 45213, USA

[c] US EPA Office of Research and Development, National Risk Management Research Laboratory, Research Triangle Park, NC 27711, USA

[d] US EPA Office of Research and Development, National Risk Management Research Laboratory, 26W Martin Luther King Dr., Cincinnati, OH 45268, USA

Abstract

Airborne black carbon from urban traffic is a climate forcing agent and has been associated with health risks to near-road populations. In this paper, we describe a case study of black carbon concentration and compositional variability at and near a traffic-laden multi-lane highway in Cincinnati, Ohio, using an onsite aethalometer and filter-based NIOSH Method 5040 measurements; the former measured 1-min average black carbon concentrations and the latter determined the levels of organic and elemental carbon (OC and EC) averaged over an approximately 2-h time interval. The results show significant wind and temperature effects on black carbon concentration and composition in a way more complex than predicted by Gaussian dispersion models.

Under oblique low winds, namely $u_x[= u \times \sin(g=q)]\sim (0,-0.5\ \mathrm{m\ s^{-1}})$, which mostly occurred during morning hours, black carbon concentrations per unit traffic flow were highest and had large variation. The variability did not always follow Gaussian dispersion but was characteristic of a uniform distribution at a near-road distance. Under all other wind conditions, the near-road black carbon variation met Gaussian dispersion characteristics. Significant differences in roadside dispersion are observed between OC and EC fractions, between $PM_{2.5}$ and $PM_{10-2.5}$, and between the morning period and rest of the day. In a general case, the overall black carbon variability at the multi-lane highway can be stated as bimodal consisting of Gaussian dispersion and non-Gaussian uniform distribution. Transition between the two types depends on wind velocity and wind angle to the traffic flow. In the order of decreasing importance, the microclimatic controlling factors over the black carbon variability are: 1) wind velocity and the angle with traffic; 2) diurnal

* Corresponding author. Tel.: +1 (0)513 556 3676; fax: +1 (0)513 556 4162. liangsg@mail.uc.edu (M.S. Liang). tim.keener@uc.edu (T.C. Keener).

Appendix B. Supplementary data

Supplementary data related to this article can be found at http://dx.doi.org/10.1016/j.atmosenv.2013.07.057.

temperature variations due to thermal buoyancy; and 3) downwind Gaussian dispersion. Combinations of these factors may have created various traffic–microclimate interactions that have significant impact on near-road black carbon transport.

Keywords

Black carbon; On-road traffic emission; Gaussian dispersion; Near-road transport; Climate change

1. Introduction

Carbonaceous particulate matter from on-road motor vehicle emissions contains organic carbon (OC) in particulate and semivolatile forms and the refractory carbon, variously referred to as ‘black,’ ‘elemental’, or ‘graphitic carbon’. The term ‘black carbon’ is generally defined as the soot component responsible for absorption of visible light (Yasa et al., 1979; Rosen et al., 1980), while elemental carbon (EC) refers to the refractory component determined by various OC–EC analysis methods. Soot is known to contain microcrystalline (i.e., graphitic) regions (e.g., Rosen and Novakov, 1977), hence the term ‘graphitic carbon.’ In this paper, ‘black carbon’ is used as general term for both light-absorbing carbon measured by an aethalometer and EC measured by NIOSH 5040 (Birch and Cary, 1996), with the latter being a principal subset of black carbon.

Airborne OC components from motor vehicle exhaust adsorb onto EC and other inorganic nuclei. In the process, black carbon size grows rapidly, by almost 10 times, approaching a micrometer (μm)-size range (Adler et al., 2010; Xiong and Friedlander, 2001). The resultant amorphous aggregates, like other fine to ultrafine particulate matter, have less airborne mobility than gaseous pollutants. Not coincidently, black carbon aerosols are found to have limited aerial extent in atmospheric distribution, relatively short atmospheric residence times of a few days to weeks, and occurrences of regional emission hotspots (e.g., Highwood and Kinnersley, 2006; Bergstrom et al., 2002; He and Dhaniyala, 2012; Liousse et al., 1996; Parungo et al., 1994).

In an urban area, transportation routes (i.e., highways, arteries and connectors) distribute and connect its population and activities. The network creates numerous configurations in traffic-wind orientations producing a diverse range of microclimate conditions. Black carbon transport in this near-surface boundary layer can be complex. Kumar et al. (2011) reviewed ultrafine aerosol transport in urban areas and outlined five urban scales of wind variability, among which aerosol transport mechanisms differ. The smallest scales in vehicle wake, highway orientation, and street canyons, can host intense and complex aerodynamic interactions affecting pollutant transport. For these reasons, observed departure from the classic Gaussian dispersion process is widely reported (Zhu et al., 2002; Finn et al., 2010; Rao et al., 2002; Levitin et al., 2005; Mishra and Padmanabhamutry, 2003; Oettl et al., 2001).

Microclimatic factors controlling near-road pollutant transport have been known for many years in road emission modeling and impact assessment (e.g., Turner, 1970; Eskridge and Rao, 1983; Venkatram, 1992, 1996; Venkatram et al., 2004, 2007; Wang et al., 2006;

Chock, 1977; Huber et al., 1991; Davidson et al., 1995; Cochran and Derickson, 2011). The effects are important to near-road air quality monitoring planning (Baldauf et al., 2009) and in air pollution mitigation such as the use of tree and vegetation barriers along roadways (e.g., Baldauf et al., 2008). Despite numerous investigations since Turner (1970) and Calder (1973), however, the near-road transport analysis of pollutants in urban settings remains a challenge. This challenge will not lessen because of occurring climate change in wind field as well as evolving urban landscape and transportation infrastructures.

As a part of the characterization and adaptation effort, we describe here a case study on the black carbon concentrations and their variability at and near a traffic-laden multi-lane highway in Cincinnati, Ohio. Discussion is centered on pollutant transport under low wind meteorological conditions. In a separate paper, we will utilize the measurements and analysis results to quantitatively evaluate Gaussian transport models in order to improve the model performance at low wind conditions. Together, these studies converge to show the importance of vertical dispersion at the road (σ_o) on the pollutant's spatiotemporal variation in a near-road environment.

2. Materials and methods

The inter-state 75 (I-75) highway segment evaluated in this study measures 794-m long between two highway overpasses. This slightly curved road consists of five traffic lanes in each direction separated by a median; the outermost two lanes are separated from the main interstate and used for by-pass traffic. On the eastern side, a highway embankment of ~0.8 m height slopes down at a ~1:10 grade to a flat concrete-paved empty open space, where five sampling stations (M_1–M_5) were aligned perpendicular to the traffic flow (Fig. 1). On the western side of the highway is a gently sloped residential area, at an average grade of 1:127 to the highway, of low-rise houses.

2.1. Traffic and wind measurements

Table 1 lists the traffic flow and meteorological conditions for each sampling period during the 9-day field study. A high definition camcorder fixed at the shoulder of the highway continuously captured on-road traffic activities. Traffic flow volume, fleet composition, and speed were later retrieved by extracting vehicular trajectory using a video-capture data collector method of Wei et al. (2005). Meteorology conditions were measured by a sonic anemometer weather station (Vantage Pro2™, Davis Instruments) at x = 30 m. The sensor of the weather station was fixed at same height as that of the sampler inlets. The date and time stamp was synchronized among the instruments, allowing temporal correlation of the traffic, weather, and black carbon measurements.

The total traffic flow on the highway was 2651 to 15,320 veh h^{-1} with an average of 9245 ± 1722 veh h^{-1}. Traffic speed varied slightly, averaging from 72.2 ± 22.3 to 99.6 ± 13.9 km h^{-1} (44.9 ± 13.9–61.9 ± 8.6 mph). Daily bi-modal traffic variation persisted for gasoline passenger vehicles (PC), with peaks during morning and afternoon rush hours, while the traffic of diesel trucks and buses (TK) peaked in the mid-day at ~600–2100 veh h^{-1}. On weekends, the morning peak hour for passenger cars occurred after 11 am and the truck volumes remained low throughout the day. In the monitoring period, the by-pass lanes

(outermost 2 lanes) carried less traffic per lane, for example, by 2.5 and 4.5 times. Nevertheless, the by-pass lanes are combined with the main highway lanes into a single linear source. Station M_1 ($x = 0$) is taken as the boundary of air pollutant dispersion toward roadside (Fig. 1).

Strong diurnal variations in air temperature (T), air density (ρ), wind velocity (u) and wind direction (θ) are characteristic of the measurement period (Fig. 2). The daily average of calm wind frequency was 11.73–53.09% between 6:30 am–8:00 pm. The highest was 78% during the 120-min 7M sampling period (Table 1). Daily average wind velocity was 0.24 ± 0.34–0.82 ± 0.81 m s^{-1}, before a 2.79 mm/24-h rainfall event (National Weather Services, Luken Airport) in the evening of October 13. Ambient wind velocity afterward increased to a maximum 6.7 m s^{-1}, with daily averages from 1.0 ± 0.8 to 2.79 ± 1.18 m s^{-1}, accompanied by reduced diurnal T and ρ variations. On other days of weak winds, a 1-min average wind direction changed frequently between downwind θ and upwind $-\theta$ (Fig. 2). Downwind refers to the wind of vector from the road to the sampling stations, and upwind is the opposite (station to road) direction. Overall, for the monitoring period, Pasquill stability class A–B (Pasquill, 1961) is assigned based on the cloudiness index and wind conditions.

For θ designation in Fig. 1, a statistical analysis shows the influence of multi-lane traffic on the near-road wind field (Fig. 3). Average u increased from 0.81–1.03 m s^{-1} to 1.66–1.96 m s^{-1}, when the upwinds along the uplane traffic, namely, the traffic in lanes adjacent to the sampling stations became sub-parallel at a small angle <60° , its variance also increased (Fig. 3a). In contrast, upwinds against the traffic had the smallest average speed 0.81–0.97 m s^{-1}. Similar wind variation in relation to traffic flow was reported by Chock (1980) and by Eskridge and Rao (1983). To describe the traffic wake effect, $\theta' = \theta$ for upwind and $\theta' = 180 - |.\theta|.$ for downwind are adopted all relative to the monitoring stations in reference to the uplane traffic. This convention specifies $\theta' < 90$ for along-traffic wind and $\theta' > 90$ for against-traffic wind in the bi-directional highway (Fig. 1).

2.2. OC–EC and black carbon quantification

2.2.1. Laboratory OC and EC analysis—Particulate samples of <2.5 mm ($PM_{2.5}$) and 2.5–10 μm ($PM_{10-2.5}$) size fractions were collected onto pre-baked quartz-fiber filters by five high-volume air samplers (Model TE-6070V, Tisch Environmental Inc.). The samplers were set up at the sampling stations M_1-M_5, one sampler at each location. The inlets of the samplers were at approximately 1.7 m above the ground. Prior to and after the field study, the five samplers were checked for leakage on-site using a pre-calibrated, variable resistance calibration kit supplied by the manufacturer.

Collected air filters were analyzed for OC and EC by NIOSH Method 5040, which is based on a thermal–optical analysis technique (Birch and Cary, 1996). Quartz-fiber filters were used for sample collection because of the high temperatures (≥850 °C) employed during the analysis. The thermal–optical analyzer (Sunset Laboratory, Inc., Oregon) was equipped with a pulsed diode laser and photodetector for continuous monitoring of filter transmittance (and reflectance). Based on the filter transmittance (reflectance), a correction for the ‘char’ formed during analysis of some materials (through carbonization) was made to reduce bias in the OC and EC results.

The total OC and EC on the filter were calculated by correction to the sample punch areas representative of a fraction of the deposit area. The OC results were also corrected to the field and laboratory OC blanks (correction for adsorbed vaporous OC). At the roadside location, M_1 (x = 0), OC concentration ranges in $PM_{2.5}$ are 2.55–9.39, 3.04–5.19, and 2.76–6.66 μg m^{-3} in the morning, noon and afternoon periods, respectively. Corresponding EC concentration ranges are 1.57–4.46, 1.59–2.51, and 1.56–2.56 μg m^{-3}. The $PM_{10–2.5}$ fraction contains less OC and EC than $PM_{2.5}$ by factors, respectively, ranging from 2.34 to 7.50 and 4.53 to 16.35. Detailed OC and EC results for all samples are provided in the Supplemental materials.

2.2.2. Black carbon aethalometer measurements—A MicroAeth aethalometer (MicroAeth™ model AE51, McGee Scientific) was used at the road curbside M_1 (z 1.7 m) to measure black carbon using the 880-nm optical absorption. Measuring principles of aethalometer and instrument calibration for BC measurements are given in Hansen et al. (1984). The time interval of the aethalometer measurements was one minute. During each sampling period of approximately 2 h, the aethalometer measurements were conducted in a staggered sequence among the four sampling stations M_1–M_4. Each measurement at a station lasted ~8 min. At least 5 stable 1-min average black carbon measurements were obtained after stabilization before relocation to the nearby station. Before field sampling, the aethalometer was calibrated, by the manufacturer, for air flow rate using an external standard air flow calibrator and for the performance of black carbon measurement following the principles described in Hansen et al. (1984).

The relationship between non-selective black carbon measurements, labeled as C_{BC}, and the total EC concentrations ($C_{EC,t}$) of $PM_{2.5}$ and $PM_{10–2.5}$ samples was examined (Fig. 4). The overall linear correlation between C_{BC} and $C_{EC,t}$ (Fig. 4) yields $C_{EC,t}$ = (0.908 ± 0.054) C_{BC} (R^2 = 0.527, p < 0.0001).

3. Results

3.1. Diurnal BC variability and wind dependence

A consistent correlation between C^*_{BC} and u or its standard deviation was observed; the traffic-normalized concentration is given by $C^*_{BC}=C_{BC}/T_r$, where T_r is the traffic volume per unit time. In Fig. 3b, arithmetic averages of all C^*_{BC} measurements range from 0.009 to 0.0255 μg $(min)^1$ $(m^3$ $veh)^{-1}$. However, for most wind angles, the C^*_{BC} averages fall into a range of 0.009–0.018 μg $(min)^1$ $(m^3$ $veh)^{-1}$. At small θ, significantly higher C^*_{BC} was observed. The largest average was 0.0255, 0.0225, and 0.0248 μg $(min)^1$ $(m^3$ $veh)^{-1}$ for the upwind θ = 40°, 62.5°, and downwind θ = 27.5°, respectively. For the winds opposing the traffic, average wind velocities were the lowest and their relative variance was the largest (Fig. 3a).

This $u \sim C^*_{BC}$ correlation is further corroborated in daily diurnal variations of meteorological parameters and black carbon levels at the M_1 location (Fig. 5). High C^*_{BC} levels in the early morning periods of still winds were followed by a rapid concentration

decrease in the day-time period. The day-time period was characteristic of increasing u and wind energy in the form of 10-min σ_{u_X}. In the evening, C^*_{BC} levels either recovered, approaching to the high levels in the morning, or remained low if wind turbulence persisted due to regional influences (Fig. 5).

3.2. Sources of OC and EC variability

3.2.1. The effect of wind velocity and angle—The 1-min average C^*_{BC} variations with wind are further examined using traffic-normalized OC and EC concentrations in the $PM_{2.5}$ and $PM_{10\text{-}2.5}$ fractions. The highest C_{OC} and C_{EC} in $PM_{2.5}$ are 9.4 ± 0.9 μg m^{-3} and 4.5 ± 0.5 μg m^{-3}, respectively. The OC and EC concentrations are at similarly high levels, 9.1 ± 1.0 μg m^{-3} and 3.7 ± 1.8 μg m^{-3}, for the 7M period of the highest calm wind frequency (~78%). In $PM_{10–2.5}$, the largest C_{OC} and C_{EC} were observed in the same time periods, but at consistently lower levels than in $PM_{2.5}$.

The wind dependence for traffic-normalized C^*_{OC} and C^*_{EC} is shown in Fig. 6. The highest C^*_{OC} and C^*_{EC} are, respectively, 0.145 and 0.039 μg $(min)^1$ $(m^3$ $veh)^{-1}$ in $PM_{2.5}$, and 0.024 and 0.006 μg $(min)^1$ $(m^3$ $veh)^{-1}$ in $PM_{10–2.5}$. These high C^* levels occurred in a narrow range of the oblique low upwinds opposing the uplane traffic, or u_X~(0, −0.50 m s^{-1}) mostly in the morning hours. Under all other wind conditions, C^*_{OC} and C^*_{EC} are confined to a broad range insensitive to wind velocity (Fig. 6). Average C^*_{OC} and C^*_{EC} in $PM_{2.5}$ are 0.031 and 0.014 μg $(min)^1$ $(m^3$ $veh)^{-1}$, respectively, or smaller by 4.6 and 2.8 times than the maximum under the oblique low upwind conditions. In $PM_{10–2.5}$, the difference is 3.4 and 4.2 times (Table 2).

3.2.2. The temperature effect—The temperature effects defined by $C^* \sim T^{-1/3}$ (Eq. (A. 11)) are distinct between the two groups identified based on the wind effects. Under oblique low upwind conditions, the largest C* concentrations and variability are found in a narrow temperature window (Fig. 7). Under other wind conditions, the black carbon variability conforms to $C^* \sim T^{-1/3}$. These data also showed the characteristics of Gaussian dispersion to be discussed next. The correlation cannot be defined for EC in $PM_{2.5}$ for this study. At location M_1, a linear regression of the $C^* \sim T^{-1/3}$ relationship yields a slope of −0.420, −0.148, and −0.203 μg $(min)^1$ $(m^3$ $veh)^{-1}$ $C^{-1/3}$ for OC in $PM_{2.5}$, OC in $PM_{10–2.5}$, and EC in $PM_{10–2.5}$, respectively. The larger slope for OC in $PM_{2.5}$ indicates more significant temperature effects on the volatile OC fraction of the finer particulate fraction.

3.3. Roadside EC and OC variability

The two types of C^*_{OC} and C^*_{EC} variability can also be identified in near-road dispersion along the M_1 to M_5 190-m transect. First, for those displaying the $C^* \sim T^{-1/3}$ relationship at M_1, the roadside C^*_{OC} and C^*_{EC} variations predominantly satisfy the Gaussian dispersion (Figs. 8 and 9a). This roadside concentration variability shows a maximum change of 0.018 μg $(min)^1$ $(m^3$ $veh)^{-1}$ for OC and 0.009 μg $(min)^1$ $(m^3$ $veh)^{-1}$ for EC in $PM_{2.5}$ (Table 2). The level of variability is only slightly smaller than that due to the temperature effects, but is

significantly smaller, by 3.13–7.13 times, than variability caused by the oblique and low upwind conditions (Table 2).

3.3.1. Gaussian transport process—Dispersion-induced roadside OC and EC variation is a function of road emission rate Q (=$T_r e_f$) corrected for u, the vertical dispersion error function $p_z(z,x/u)$ and its downwind equivalent $p_y(y,x/u)$ (Weil et al., 1997):

$$C=\frac{T_r e_f}{u} p_z\left(z,\frac{x}{u}\right) p_y\left(y,\frac{x}{u}\right) \quad (1)$$

Deriving from Eq. (1), the Pasquill–Gifford–Turner (PGT) and the surface-layer similarity theory (SST) analytical formulations (Luhar and Patil, 1989; Venkatram, 1992, 1996) are used to examine the observed roadside black carbon variability. Both have similar

Gaussian forms, but differ in σ_z and σ_y definition. Their traffic normalized concentration C^* = C/T_r and the concentration ratios are

$$C^*_{GPT}=\frac{e_f}{2\sqrt{2\pi}u\cdot sin\,\theta}\times\left\{\frac{1}{(a+bx)^c}\left[exp\left(-\frac{(z-h_o)^2}{2(a+bx)^{2c}}\right)\right]\right\}\xi'(x,y) \quad (2)$$

$$C^*_{SST}=\frac{e_f}{2\sqrt{2\pi}\cdot usin\,\theta}\times\frac{1}{\sigma_o(1+\varphi)}exp\left[-\left(\frac{z-h_o}{\sqrt{2}\sigma_o}\frac{1}{1+\varphi}\right)^2\right]\xi(y,x) \quad (3)$$

$$\left(\frac{C^*_x}{C^*_o}\right)_{PGT}=\frac{1}{(1+bx/a)^c}exp\left\{\left[\frac{(z-h_o)}{\sqrt{2}a^c}\right]^2\frac{(1+bx/a)^{2c}-1}{(1+bx/a)^{2c}}\right\}\times\zeta'(x,y) \quad (4)$$

$$\left(\frac{C^*_x}{C^*_o}\right)_{SST}=\frac{1}{1+\varphi}exp\left\{\left[\frac{(z-h_o)}{\sqrt{2}\sigma_o}\right]^2\frac{(1+\varphi)^2-1}{(1+\varphi)^2}\right\}\times\zeta(y,x) \quad (5)$$

The four error function terms $\zeta(y,x)$, $\zeta'(y,x)$, $\xi(y,x)$, $\xi'(y,x)\approx 1$ for near-road at x(0, 190 m) in the 794-m long highway segment. Dimensionless parameter $\varphi\approx\varphi' x$ for |L| >20 m where φ' is a dispersion factor depending on u, u^* and σ_o (Appendix Eqs. A.4 to A.6). Fig. 8 shows the least square non-linear regression results using Eq. (5) for EC in 14N and for OC in 7A. The C^*_{OC} and C^*_{EC} variability during downwind conditions conforms to the SST formulation. The Gaussian-type variability is also apparent for upwind conditions of high velocities, or $|u_x|$ > 0.8 m s^{-1} (Fig. 9a).

In both wind conditions, the concentration change in roadside Gaussian dispersion is distinct between EC and volatile OC, and between black carbon in $PM_{2.5}$ and $PM_{10-2.5}$. It can be derived from Eq. (3) that at M_1 (x = 0), the ratio C^*_{OC}/C^*_{EC} is only a function of e_f and σ_o. Not coincidently, the measured concentration ratios in the morning low winds falls into a range of 2.1–4.1 (2.9 ± 0.7, $m \pm \sigma$, N = 8) in $PM_{2.5}$, and 3.9–15.5 (6.8 ± 3.7,$m \pm \sigma$, N = 8) in

$PM_{10-2.5}$. For winds $u_x > 0.8$ m s^{-1}, the ratios are approximately 50% smaller at 1.4 ± 0.2 (N = 5) and 3.5 ± 0.7 (N = 5). This difference implies a suppression of compositional and size-dependent variability under higher wind velocity.

The initial difference in C^*_{OC}/C^*_{EC} at x = 0 was further amplified in roadside dispersion. For those showing Gaussian dispersion profiles in Figs. 8 and 9a, the C^*_{OC}/C^*_{EC} ratio increased with distance x. This change is measured by $R\%$, the percentage difference of the OC/EC ratio at a distance compared to the ratio at x = 0:

$$R\% = \frac{\left(C^*_{OC}/C^*_{EC}\right)_0 - \left(C^*_{OC}/C^*_{EC}\right)_x}{\left(C^*_{OC}/C^*_{EC}\right)_0} \cong \frac{\left(\varphi'_{EC} - \varphi'_{OC}\right)x}{1+\varphi'_{OC}x} \quad (6)$$

The dispersion-induced change in black carbon composition at roadside is shown in Fig. 10a. Gaussian dispersion at the roadside apparently led to OC enrichment relative to EC over a short distance. This is well expressed by the nature of the logistic function in Eq. (6). Magnitude of the compositional change directly depends on relative dispersivity between OC and EC or $\varphi'_{OC}/\varphi'_{EC}$. Hence it is a function of the microclimatic parameters u^*, u, and vertical dispersion at the road σ_o (Appendix Eq. (A.6)).

3.3.2. Non-Gaussian roadside transport—Non-Gaussian variations are found in black carbon concentration and composition under the oblique low upwind conditions, or u_x~(0, −0.50 m s^{-1}), which occurred mostly during the morning hours. OC and EC concentrations and compositions have several distinct properties: high C^* levels and large variance within a narrow range of wind conditions (Fig. 6); the absence of C^*~$1/T^{1/3}$ correlation in contrast to those characteristics of the Gaussian dispersion (Fig. 7); and a small increase of OC/EC ratios or $R\%$ along the near-road 190-m transect (Fig. 10b). At roadside, the geometric mean of C^*_x/C^*_0 ranges from 1.04 to 1.15 (Fig. 9b) inferring a uniform distribution $P_u(\theta)$.

Non-Gaussian upwind transport of pollutants has been reported in several studies including GM experiments (Chock, 1977, 1978), the Prairie Grass experiments (van Ulden, 1978), and in the original analysis of Turner (1970) and reanalysis of Calder (1973). In the GM experiment, higher pollutant concentrations during upwind conditions were associated with high frequency eddies which occurred when the ambient wind opposed the uplane traffic (Chock, 1980). Such meandering-induced upwind dispersion was also reported by Thoma et al. (2008) in roadside measurements and by Davidson et al. (1995) in experimental simulations.

In diagnosis, the meandering differs from atmospheric disturbance in a distinct $\sigma'_\theta \sim 1/u$ relationship; σ'_θ is the standard deviation of vertical wind directions (Hanna, 1983). Fig. 11 shows the relationship in which the standard deviation of overall wind σ_θ is used. All noon–afternoon samples conform to a region defined by two σ_θ~$1/u$ data regression lines. The morning samples, 14M and 15M, of high winds also fall into the overall trends. In contrast, all the other morning hours define a large σ_θ range below the atmospheric turbulence trend

lines. The small scales of turbulence energy (σ_θ) and low upwind ($u < 0.5$ m s^{-1}) condition favored a meandering condition, under which the exceptionally high black carbon concentrations occurred in the non-Gaussian dispersion (See Figs. 7 and 9b).

4. Discussions: microclimate factors and assessment implications

4.1. Wind factors in near-road transport

Two major types of black carbon variability in relation to the wind conditions were observed in the I-75 highway experiments:

- High and variable near-road black carbon concentrations under oblique low upwinds opposing the traffic, or u_x~(0, −0.50 m s^{-1}). Their variability, greatest during morning hours, is inconsistent with the $C^* \propto 1/T^{1/3}$ relationship at-road, but is characteristic of the roadside non-Gaussian dispersion.

- Gaussian-type black carbon variations under all other wind conditions. The near-road concentration variability conforms to Gaussian dispersion in the SST formulation. The dispersion-induced concentration difference along the 190-m M_1–M_5 transect is the smallest compared to the at-road changes caused by oblique low winds and temperatures.

Venkatram et al. (2004) proposed dual mechanisms applicable to a highway environment. The hybrid overall formulation is used in the regulatory AERMOD model (Cimorelli et al., 2004). Modified from Venkatram et al. (2004), overall black carbon concentrations at the I-75 site is written as the sum of a Gaussian dispersion component and a uniform distribution $P_u(\theta)$:

$$\frac{\overline{C}^*}{T_r} = \frac{e_f}{2\pi\sigma_o}\left[f_\theta p_z\left(z, \frac{x}{u}\right) p_y\left(y, \frac{x}{u}\right) + (1 - f_\theta)\, P_u(\theta)\right] \quad (7)$$

where f_θ is a binary proportionality factor marking a transition between the two controlling processes.

In the I-75 study, a rapid transition from Gaussian to non-Gaussian uniform distribution was observed at a small angle θ' and under low winds. Fig. 12 shows the transition in a correlation between black carbon concentrations in $PM_{2.5}$ and the overall wind standard deviation σ_w' representing the wind turbulent energy. Venkatram et al. (2007) used the vertical wind component σ_w and stipulated an inverse relationship $C^* \sim 1/\sigma_w$ that governs the near-road pollutant transport. In Fig. 12, the overall C^*_{OC} and C^*_{EC} variation envelops can be described mathematically using the relationship $C^* \sim 1/\sigma_w'$. The representation is unsatisfactory, however, under both high and low wind conditions.

A rapid transition at $\sigma_w' \sim 0.4$ m s^{-1}, or $u_x \sim$ (−0.42, 0.36 m s^{-1}) in Fig. 12 is noteworthy. Above the threshold, measured C^*_{OC} and C^*_{EC} fall into a narrow range and conform to near-road Gaussian dispersion (See Figs. 8 and 9a). On the other hand, the weaker wind energy

for $\sigma_w' < \sim 0.4 \quad \mathrm{m\,s^{-1}}$ corresponds with the elevated C_{OC}^{*} and large C_{OC}^{*} variations under the oblique low upwind conditions (Fig. 12). A uniform distribution is inferred (Fig. 9b).

The precise mechanism for this rapid transition is not immediately clear. In one possibility, the oblique low winds in a small θ' against the traffic can yield shear tensor τ_o and friction velocity $u^* \left(=\sqrt{\tau_o/p_a}\right)$, and consequently a large uplift of air mass in σ_o at the road (Appendix Eqs. A.4 to A.6). This uplift forced the emissions into a meandering state, moving toward the roadside during the morning hours. Similarly, Oettl et al. (2001) found in highway experiments that the largest model error of Gaussian formulations occurred in small θ (<25°) at opposing low wind (u~1.5 m s^{-1}). This condition was also reported in the earlier studies (e.g., Chock, 1980; Rao et al., 2002; Levitin et al., 2005). In corroborating these accounts, we suggest that the transition between two processes occurs at a small θ', but not under $\theta' \sim 0$ or parallel winds that Luhar and Patil (1989) assumed for $u \times \sin(\theta) \rightarrow 0$ in the PGT dispersion models.

The preceding discussions indicate the importance of σ_o in the at-road process that affected near-road black carbon transport. This can be seen from the fact that both PGT and SST Gaussian models (Eqs. (2)–(5)) have similar Gaussian forms, but differ in that the wind and microclimatic factors on σ_o are considered. In the PGT model, σ_o is fixed for a given stability class. In the SST formulation, σ_o is a function of dispersion factor ϕ', and hence the microclimate variables in u, u^*, and L (Appendix Eqs. A.4 to A.6).

Urban-scale and regional factors affect local microclimate conditions and thus the black carbon transport and variability. Monitoring and characterizing the near-road wind field including the vertical wind velocities and turbulent kinetics (Baldauf et al., 2009), is critical to quantifying σ_o at the road and to assess the likelihood of meandering occurrence (Anfossi et al., 2007; Timm et al., 2009). The results, as demonstrated here, are essential to assess the black carbon mobility, source strength, and spatiotemporal distribution relative to roadside receptors.

5. Conclusions

The field study and qualitative analysis at a multi-lane highway segment in Cincinnati, Ohio, point to the important roles of local wind field and microclimate conditions in the near-road black carbon transport, concentration and composition. The slightly curved highway is composed of five lanes in each direction, carrying a traffic flow of weekly and daily variations in passenger cars, heavy diesel trucks and buses that varies by day of the week and hour of the day. Black carbon air filter samples were collected at approximately 2-h averages at five near-ground stations in a 190-m transect perpendicular to the roadway. The 1-min average black carbon concentrations were also measured at the roadside.

Microclimate factors, particularly wind velocity and angle, significantly affected the black carbon concentration and composition in the near-road environment. Major conclusions of the case study are:

■ Microclimate factors (T, u, ρ) and traffic flows all show strong diurnal variations. These diurnal variations are correlated with the 1-min average black carbon concentration C_{BC} at roadside station M_1. Measured black carbon concentration in the 190-m roadside transect ranged widely from 4.04 to 52.0 μg m^{-3}. The highest C_{OC} and C_{EC} in ~2-hr sampling period are 9.4 ± 0.9 μg m^{-3} and 4.5 ± 0.5 μg m^{-3} in $PM_{2.5}$, respectively (See Supplemental materials).

■ At roadside station M_1, black carbon concentration normalized to traffic flow $C^*=(C/T_r)$ varied significantly under oblique low upwind conditions, or $u_x[= u \times \sin(\theta)]\sim(0, -0.4\ m\ s^{-1})$, mostly during the morning hours Fig. 6). Under these conditions, the highest C^*_{OC} and C^*_{EC} are, respectively, 0.145 and 0.039 μg $(min)^1$ $(m^3\ veh)^{-1}$ in $PM_{2.5}$, and 0.024 and 0.006 μg $(min)^1$ $(m^3\ veh)^{-1}$ in $PM_{10–2.5}$. The roadside OC and EC variability is consistent with a uniform distribution $P_u(\theta)$ for which the likely transport mechanism of meandering is inferred.

■ Under all other wind conditions, air temperature is the second largest controlling factor of black carbon variability. There exists a strong $C^*\sim 1/T^{1/3}$ relationship at station M_1, particularly for OC and finer $PM_{2.5}$ fractions. The temperature-dependent variability is slightly larger than those caused by roadside Gaussian dispersion within the 190-m transect. It is significantly smaller, however, than those caused by the oblique low winds.

■ Under all other wind conditions, Gaussian dispersion attenuates black carbon concentration and increases C^*_{OC}/C^*_{EC} ratios in the observed roadside transport. The average C^*_{OC} and C^*_{EC} change in the 190 m transect is respectively 0.015 and 0.010 μg $(min)^1$ $(m^3\ veh)^{-1}$ in $PM_{2.5}$. The variation is over 5 times smaller in $PM_{10–2.5}$. The magnitude of the concentration change is the smallest compared to wind and temperature factors at the road. The variability can be adequately described using the SST dispersion formulation with $\sigma_o \neq 0$ at the highway.

These results all demonstrate the importance of initial vertical dispersion σ_o at the road caused by plume rise in response to the wind–traffic interactions. For overall black carbon variations, we suggest the adaptation of Venkatram et al. (2007) in that a binary proportionate factor f_θ is used to describe the rapid transition between Gaussian dispersion and non-Gaussian transport. The f_θ definition depends on the wind–traffic interactions and microclimate factors in urban-scale and regional environments, for which further investigations are warranted.

Supplementary Material

Refer to Web version on PubMed Central for supplementary material.

Acknowledgment

The authors sincerely thank Zhuo Yao, Hao Liu, Jiangchuan Hu and Beizhao for their generous support in field investigation and data processing and are grateful to Dr. Vlad Isakov of EPA, Drs. Pratim Biswas of Washington University in St. Louis, and Drs. Heng Wei, Mingming Lu, and Xinhao Wang of the University of Cincinnati, for their technical review and constructive comments. Field sampling and characterization of this research were funded and conducted under EPA contract EP-006-011. The authors acknowledge the use of NIOSH laboratories,

Cincinnati, Ohio, for OC–EC analyses. The research described herein has been subjected to technical and administrative review by US EPA and CDC/NIOSH, and has been approved for external publication. Any opinions expressed in this paper are those of the authors and do not necessarily reflect the views of the Agencies; therefore, no official endorsement should be inferred. Mention of company name or product does not constitute endorsement by EPA or CDC/NIOSH.

Appendix A

A). For a line source at a single-lane highway, black carbon C^* at x is (Luhar and Patil, 1989):

$$C^*=\frac{e_f}{u\cdot sin\,\theta}\left\{\frac{1}{2\sqrt{2\pi}\sigma_z}\left[exp\left(-\frac{(z-h_o)^2}{2\sigma_z^2}\right)+exp\left(-\frac{(z+h_0)^2}{2\sigma_z^2}\right)\right]\right\} \times\left[\left(\frac{sin\,\theta\,(p-y)-xcos\,\theta}{\sqrt{2}\sigma_y}\right)+erf\left(\frac{sin\,\theta\,(p+y)+xcos\,\theta}{\sqrt{2}\sigma_y}\right)\right] \quad (A.1)$$

In the PGT formulation, σ_y, σ_z are defined by parameters a, b, c, p, and q for under stability class A–B for which the black carbon C^*_{PGT} and concentration ratio $(C^*_x/C^*_0)_{PGT}$ are:

$$C^*_{PGT}=\frac{e_f}{2\sqrt{2\pi}u\cdot sin\,\theta} \times\left\{\frac{1}{(a+bx)^c}\left[exp\left(-\frac{(z-h_o)^2}{2(a+bx)^{2c}}\right)\right]\right\} \times\left[erf\left(\frac{sin\,\theta\,(p-y)-xcos\,\theta}{\sqrt{2}p\sqrt{1+qx}}\right)+erf\left(\frac{sin\,\theta\,(p+y)+xcos\,\theta}{\sqrt{2}p\sqrt{1+qx}}\right)\right] \quad (A.2)$$

$$\left(\frac{C^*_x}{C^*_0}\right)_{PGT}=\frac{1}{(1+bx/a)^c}exp\left\{\left[\frac{(z-h_o)}{\sqrt{2}a^c}\right]^2\frac{(1+bx/a)^{2c}-1}{(1+bx/a)^{2c}}\right\}\times\xi\,(x,y) \quad (A.3)$$

Adapting from the SST formulation of Venkatram (1996, 1992), we can write σ_z for stability class A–B assuming $\sigma_o \neq 0$:

$$\sigma_z=\sigma_o+\varphi\sigma_o \quad (A.4)$$

$$\varphi=\varphi' x\sqrt{\left[1+0.006\left(\frac{x}{|L|}\right)^2\right]} \quad (A.5)$$

$$\varphi'=\sqrt{\frac{2}{\pi}}\frac{u*}{u\sigma_o} \quad (A.6)$$

Substituting Eqs. A.4 and A.5 into A.1, the SST Gaussian formulation for black carbon concentration and concentration ratios can be written as:

$$C^*_{SST}=\frac{e_f}{2\sqrt{2\pi}\cdot usin\,\theta}\times\frac{1}{\sigma_o\,(1+\varphi)}exp\left[-\left(\frac{z-h_o}{\sqrt{2}\sigma_o}\frac{1}{1+\varphi}\right)^2\right]\times\left[erf\left(\frac{sin\,\theta\,(p-y)-xcos\,\theta}{\sqrt{2}p\sqrt{1+qx}}\right)+erf\left(\frac{sin\,\theta\,(p+y)+xcos\,\theta}{\sqrt{2}p\sqrt{1+qx}}\right)\right] \quad (A.7)$$

$$\left(\frac{C^*_x}{C^*_o}\right)_{SST}=\frac{1}{1+\varphi}exp\left\{\left[\frac{(z-h_o)}{\sqrt{2}\sigma_o}\right]^2\frac{(1+\varphi)^2-1}{(1+\varphi)^2}\right\}\times\xi\,(y,x) \quad (A.8)$$

B). For multi lanes of “air puff” each as an independent source, *C** at *x* is an integration over the highway (*x*, *x* + *W*) (Venkatram et al., 2007),

$$C^*_x=\int_x^{x+W}\frac{e_f}{b+a\sigma_w x}A\,\mathrm{d}x=\frac{T_r e_f}{W\sigma_w}\frac{A}{a}ln\left[\frac{b+a\sigma_w\,(x+W)}{b+a\sigma_w}\right] \quad (A.9)$$

C). For well-mixed air parcel at a multi-lane highway, σ_o in Eqs. A.7 and A.8 is given using the geometric similarity:

$$\sigma_o=\sqrt{\frac{u_D^2+u_w^2}{u_x^2}}W\approx\frac{u_w}{u_x}\quad\text{for}\quad Wu_D\ll u_w \quad (A.10)$$

u_w~$1/T^3$ for thermal plume rise in convective boundary layer (Weil, 1985). Then Eq. A.10 yields $\sigma_o \propto WT^{1/3}$. Substituting the relationship into Eq. A.7 and further assuming the error function terms ~1 for near-road stations, we have:

$$C^*_{SST}\Big|_{x=0}\propto\frac{e_f}{WT^{1/3}} \quad (A.11)$$

Nomenclature

a, b, c, p, q	Pasquill's stability parameters
C	concentration (M l^{-3}) with subscript referring to EC, OC, or BC
C_o	concentration (M l^{-3}) at M_1 at the highway curbside taken as the road source concentration
C*	concentration (EC, OC, or BC) normalized to traffic flow in Mt $(l^3 Veh)^{-1}$
e_f	effective emission factor, dimensionless
g	gravitational acceleration constant
h_o	source height = in l

H	air emission height at tail pipe in l
H_p	plume rise height at road in l
L	Monin–Obhukov length in l
p	a half length of the road segment taken as a line source in l
P_z, P_y	a half length of the road segment taken as a line source in l
Q_o	surface heat flux in J/t A^{-1}
R%	the percentage difference of the OC/EC ratio at a distance compared to the ratio at $x = 0$
T	ambient air temperature in T
T_r	traffic volume per unit time in Veh t^{-1}
u	wind velocity in l t^{-1}
u_x	wind velocity in downwind direction in l t^{-1}
u*	surface friction velocity related to vertical temperature gradient and air density in l t^{-1}
W	Highway width in l
α	constant depending on W, z, h_o and ϕ for given air parcel
θ	angle between road and wind direction in Fig. 1
θ'	a conversion of θ to describe the traffic wake effect ρ air density in M l^{-3}
σ_x, σ_y, σ_z	dispersion parameters in x, y, z directions in l
σ_o	vertical dispersion parameter at $x = 0$ in l
σ_W	vertical velocity variance in l t^{-1}
σ'_w	overall wind velocity variance in l t^{-1}
σ_θ	standard deviation of wind angle θ
ϕ	dimensionless parameter
ϕ′	dispersion parameter depending on microclimatic factors in l^{-1}

References

Adler G, Riziq AA, Erlick C, Rudich Y. Effect of intrinsic organic carbon on the optical properties of fresh diesel soot. PNAS. 2010; 107(15):6699–6704. [PubMed: 20018649]

Anfossi A, Oettl D, Degrazia G, Goulart A. An analysis of sonic anemometer observations in low wind speed conditions. Boundary-Layer Meteorology. 2007; 114(1):171–203.

Baldauf R, Thoma E, Khlystov A, Isakov V, Bowker G, Long T, Snowe R. Impacts of noise barriers on near-road air quality. Atmospheric Environment. 2008; 42:7501–2507.

Baldauf R, Watkins N, Heist D, Bailey C, Rowley P, Shores R. Near-road air quality monitoring: factors affecting network design and interpretation of data. Air Quality Atmospheric Health. 2009; 2:1–2.

Bergstrom RW, Sussell PB, Hignett P. Wavelength dependence of the absorption of black carbon particles: predictions and results from the TARFOX experiment and implications for the aerosol single scattering albedo. Journal of the Atmospheric Sciences. 2002; 59:561–277.

Birch ME, Cary RA. Elemental carbon-based method for monitoring occupational exposures to particulate diesel exhaust. Aerosol Science and Technology. 1996; 25:221–241.

Calder KL. On estimating air pollution concentrations from a highway in an oblique wind. Atmospheric Environment. 1973; 7:861–268.

Chock DP. General motors sulfate dispersion experiment – an overview of the wind, temperature, and concentration fields. Atmospheric Environment. 1977; 11:551–259.

Chock DP. A simple line-source model for dispersion near roadways. Atmospheric Environment. 1978; 12:821–229.

Chock DP. General motors sulfate dispersion experiment: an analysis of the wind field near a road. Boundary-Layer Meteorology. 1980; 18:431–251.

Cimorelli AJ, Perry SG, Venkatram A, Weil JC, Paine RJ, Wilson RB, Lee RF, Peters WD, Brode RW, Paumier JO. AERMOD: Description of Model Formulation. 2004:89. EPA-454/R-03-004.

Cochran L, Derickson R. A physical modeler's view of computational wind engineering. Journal of Wind Engineering and Industrial Aerodynamics. 2011; 99:131–253.

Davidson MJ, Mylne KR, Jones CD, Phillips JC, Perkins RJ, Fung JCH, Hunt JCR. Plume dispersion through large groups of obstacles – a field investigation. Atmospheric Environment. 1995; 29(22): 3241–2256.

Eskridge RE, Rao ST. Measurement and prediction of traffic-induced turbulence and velocity fields near roadways. Journal of Climate and Applied Meteorology. 1983; 22:1431–2443.

Finn D, Clawson KL, Carter RG, Rich JD, Biltoft C, Leach M. Analysis of urban atmosphere plume concentration fluctuations. Boundary-Layer Meteorology. 2010; 136:431–245.

Hanna SR. Lateral turbulence intensity and plume meandering during stable conditions. Journal of Climate and Applied Meteorology. 1983; 22:1421–2430.

He M, Dhaniyala S. Vertical and horizontal concentration distributions of ultrafine particles. Atmospheric Environment. 2012; 46:221–236.

Hansen ADA, Rosen H, Novakov T. The aethalometer – an instrument for the real-time measurement of optical absorption by aerosol particles. The Science of the Total Environment. 1984; 36:191–296.

Highwood EJ, Kinnersley RP. When smoke gets in our eyes: the multiple impacts of atmospheric black carbon on climate, air quality and health. Environment International. 2006; 32:561–266.

Huber AH, Arya SP, Rajala SA, Borek JW. Preliminary studies of video images of smoke dispersion in the near wake of a model building. Atmospheric Environment. 1991; 25A(7):1191–2209.

Kumar P, Ketzel M, Vardoulakis S, Pirjola L, Britter R. Dynamics and dispersion modelling of nanoparticles from road traffic in the urban atmospheric environment–a review. Journal of Aerosol Science. 2011; 42:581–203.

Levitin J, HärkÖnen J, Kukkonen J, Nikmo J. Evaluation of the CALINE4 and CAR-FMI models against measurements near a major road. Atmospheric Environment. 2005; 39:4431–2452.

Liousse C, Penner JE, Chuang C, Walton JJ, Eddleman H, Cachier H. A global three-dimensional model study of carbonaceous aerosols. Journal of Geophysical Research. 1996; 101(D14):19411–29432.

Luhar AK, Patil RS. A general finite line source model for vehicular pollution prediction. Atmospheric Environment. 1989; 23(3):551–262.

Mishra VK, Padmanabhamutry B. Performance evaluation of CALINE3, CAL3QHC and PART5 in predicting lead concentration in the atmosphere over Delhi. Atmospheric Environment. 2003; 37:3071–2089.

Oettl D, Kukkonen J, Alfons Almbauer R, Sturm PJ, Pohjola M, Härkönen J. Evaluation of a Gaussian and a Lagrangian model against a roadside data set, with emphasis on low wind speed conditions. Atmospheric Environment. 2001; 35:2121–2132.

Parungo P, Nagamoto C, Zhou M-Y, Hansen ADA, Harris J. Aeolian transport of aerosol black carbon from China to the ocean. Atmospheric Environment. 1994; 28(20):3251–2260.

Pasquill F. The estimation of the dispersion of windborne material. Meteorite magazine. 1961; 90:31–29.

Rao KS, Gunter RL, White JR, Hosker RP. Turbulence and dispersion modeling near highways. Atmospheric Environment. 2002; 36:431–2346.

Rosen H, Novakov T. Raman scattering and the characterization of atmospheric aerosol particles. Nature. 1977; 266:701–210.

Rosen H, Hansen ADA, Dod RL, Novakov T. Soot in urban atmospheres: determination by an optical absorption technique. Science. 1980; 208:741–244. [PubMed: 17771130]

Timm AU, Degrazia GA, Roberti DR, Anfossi D. Employing turbulent and meandering time scales to modeling the contaminants enhanced horizontal dispersion. Atmospheric Research. 2009; 93:811–217.

Thoma ED, Shores RC, Isalov V, Baldauf RW. Characterization of near-road pollutant gradients using path-integrated optical remote sensing. Journal of the Air & Waste Management Association. 2008; 58:871–290.

Turner, DB. Workbook of Atmospheric Dispersion Estimates. National Air Pollution Control Administration; Cincinnati, Ohio: 1970. p. 83

van Ulden AP. Simple estimates for vertical diffusion from sources near the ground. Atmospheric Environment. 1978; 12:2121–2129.

Venkatram A. Vertical dispersion of ground-level releases in the surface boundary layer. Atmospheric Environment. 1992; 26A(5):941–249.

Venkatram A. An examination of the Pasquill–Gifford–Turner dispersion scheme. Atmospheric Environment. 1996; 30(8):1281–2290.

Venkatram A, Isakov V, Jing Y, Pankratz D. Modeling dispersion at distances of meters from urban sources. Atmospheric Environment. 2004; 38:4631–2641.

Venkatram A, Isakov V, Thoma E, Baldauf R. Analysis of air quality data near roadways using a dispersion model. Atmospheric Environment. 2007; 41:9481–2497.

Wang JS, Chan TL, Cheung CS, Leung CW, Hung WT. Three-dimensional pollutant concentration dispersion of a vehicular exhaust plume in the real atmosphere. Atmospheric Environment. 2006; 40:481–297.

Wei H, Feng C, Meyer E, Lee J. Video-capture-based approach to extract multiple vehicular trajectory data for traffic modeling. Journal of Transportation Engineering. 2005; 131(7):491–205.

Weil JC. Updating of applied diffusion models. Journal of Applied Meteorology. 1985; 24(11):1111–2130.

Weil JC, Corid LA, Brower RP. A PDF dispersion model for buoyant plumes in the convective boundary layer. Journal of Applied Metrology. 1997; 36:981–2003.

Xiong C, Friedlander SK. Morphological properties of atmospheric aerosol aggregates. PNAS. 2001; 98(21):11851–21856. [PubMed: 11592995]

Yasa Z, Amer NM, Rosen H, Hansen ADA, Novakov T. Photoacoustic investigations of urban aerosol particles. Applied Optics. 1979; 18:2521–2530.

Zhu Y, Hinds WC, Kim S, Shen S. Study of ultrafine particles near a major highway with heavy-duty diesel traffic. Atmospheric Environment. 2002; 36:4323–4433.

HIGHLIGHTS

- Microclimates dominate near-road black carbon transport from multi-lane highways.
- Highest BC, EC and OC occurred during oblique low upwind mostly in early morning.
- Other wind conditions permit Gaussian dispersion of different EC and OC mobility.
- Wind and temperature dependent σ_o significantly affects roadside dispersion.
- The microclimate effects in urban settings have implication to black carbon assessment.

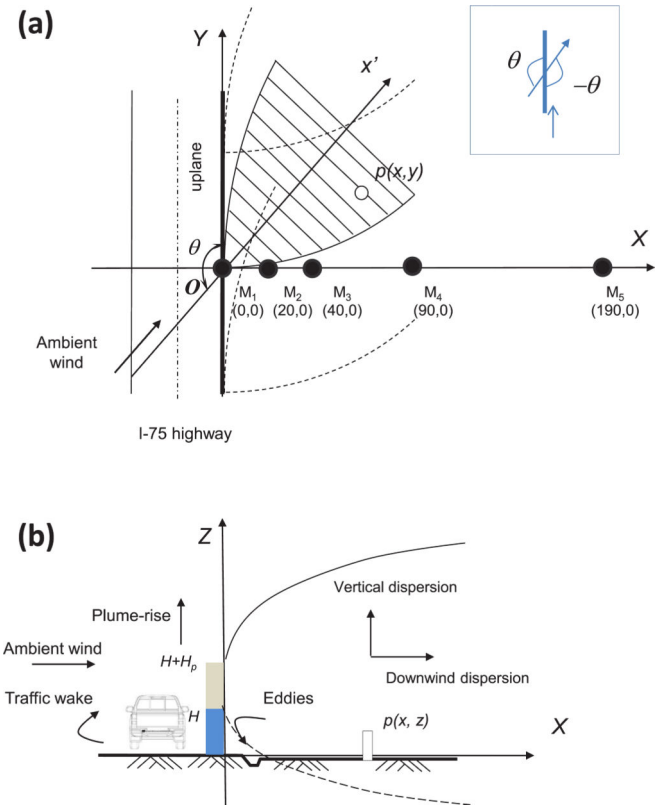

Fig. 1.

a) artisan coordinates of the highway and monitoring stations (in m) showing geometric relationships between air plumes (solid and dashed lines), wind, traffic and M_1–M_5 transect; b) black carbon transport in cross-section with major mechanisms marked for a receptor $p(x,z)$ in a flat open area.

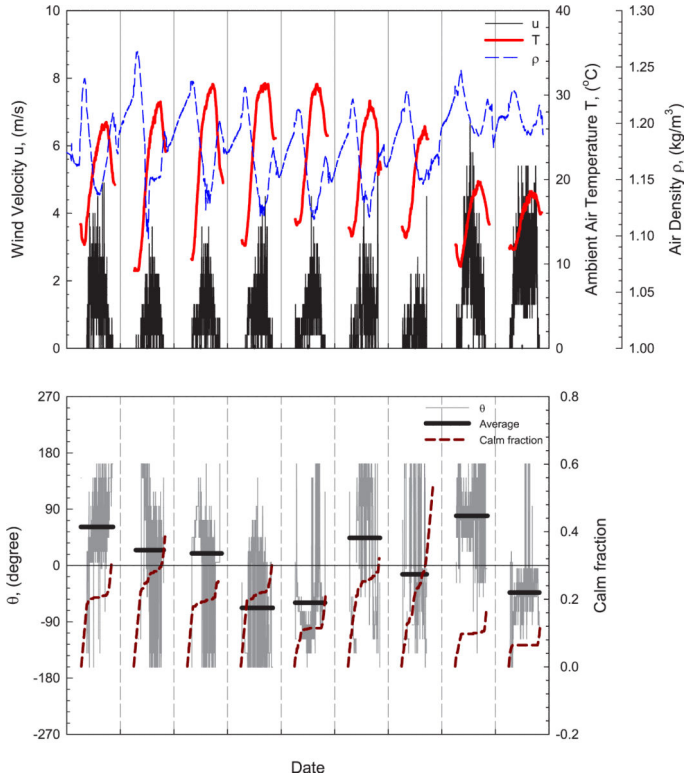

Fig. 2.

Diurnal variations of u, θ, T, ρ, and daily accumulative calm fraction. θ is the angle between the road and wind direction in Fig. 1.

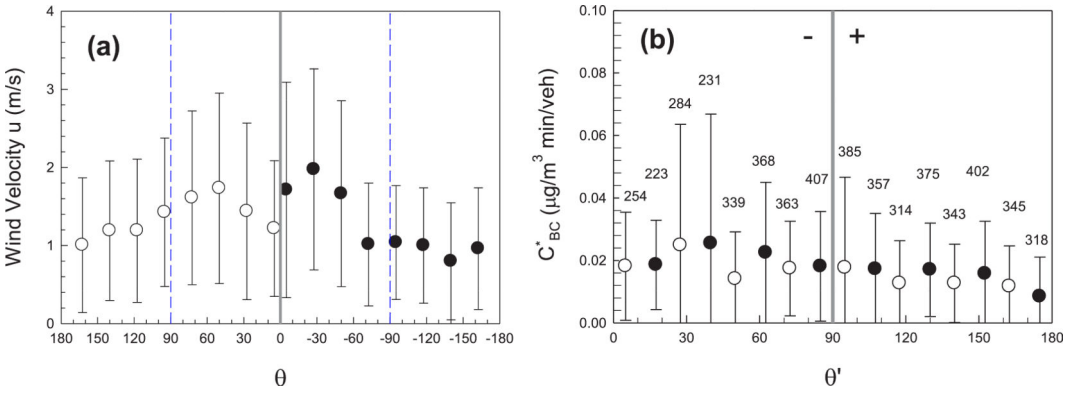

Fig. 3.

Statistics of u and C^*_{BC} at M_1 station for the monitoring periods. Numbers of minutely measurements are marked. " + " and " − " indicate wind along and counter traffic in uplane. θ is the angle between road and wind direction. θ' is the conversion of θ to describe the traffic wake effect. C^*_{BC} is BC concentration normalized to the traffic flow.

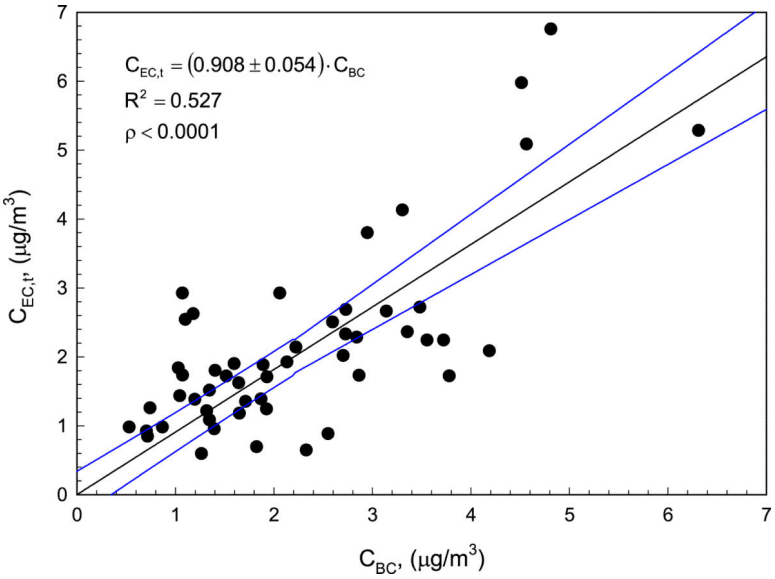

Fig. 4.

Correlation between C_{BC} and $C_{EC,t}$ at same locations.

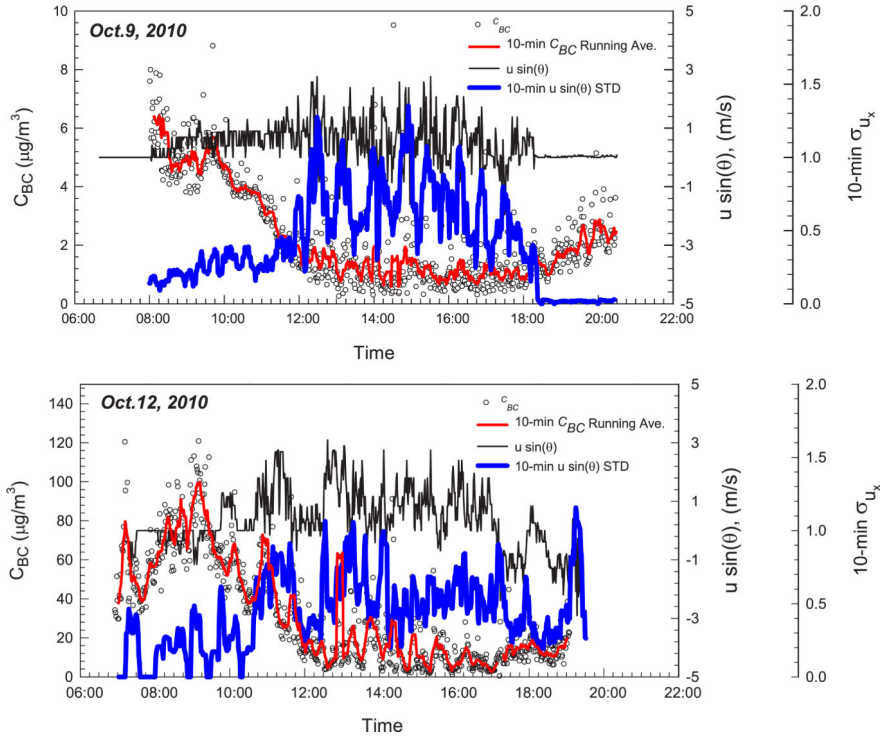

Fig. 5.

Typical diurnal daily variation of C_{BC} (circle), $u \times \sin\theta$ (line), and its 10-min standard variance (STD) (heavy line). The 10-min C_{BC} running average is also shown.

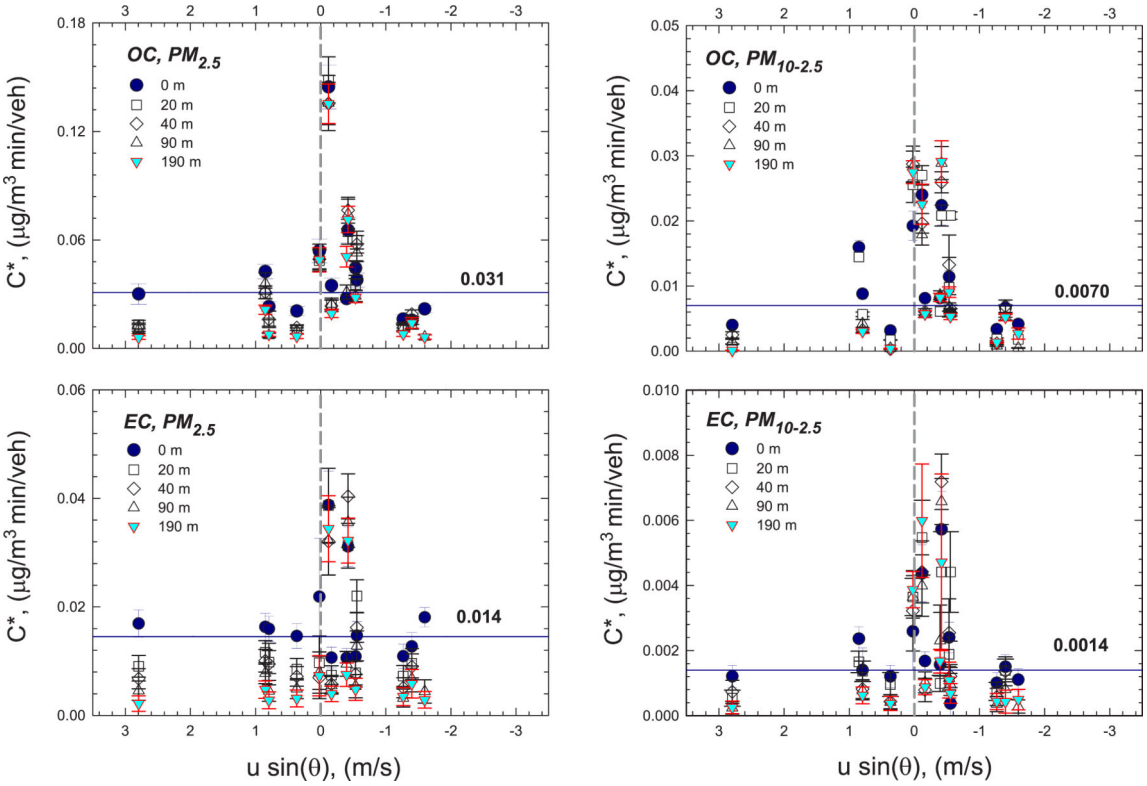

Fig. 6.

C^*_{OC} and C^*_{EC} as a function of u sin θ. Horizontal bar and number indicate C^*_{OC} or C^*_{EC} averages of samples at M_1 (x = 0) excluding those under oblique low upwinds. Error bar is 1σ uncertainty C^*_{OC} and C^*_{EC} and are normalized concentrations to the traffic flow.

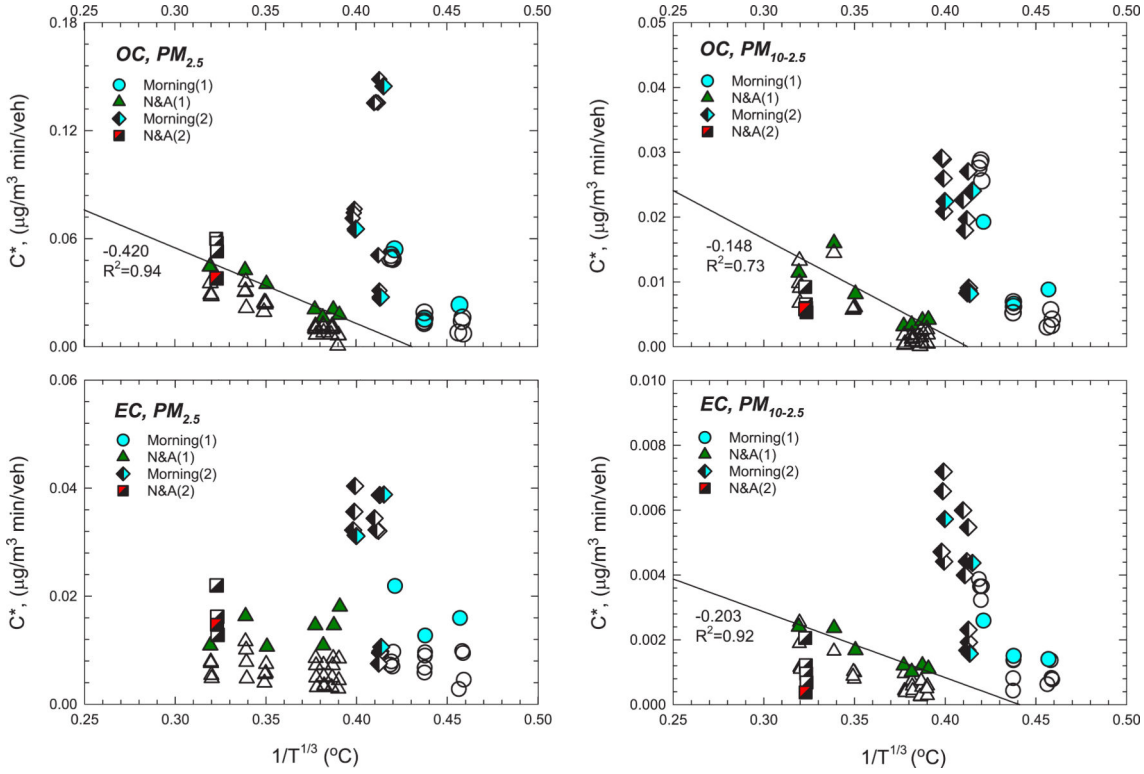

Fig. 7.

C^*_{OC} and C^*_{EC} variations with temperature at M_1 (solid symbols) and M_2–M_5 (open). Labels in legend: N&A – noon–afternoon; (1) – Gaussian dispersion; (2) – non-Gaussian dispersion. Regression slope and R^2 are marked.

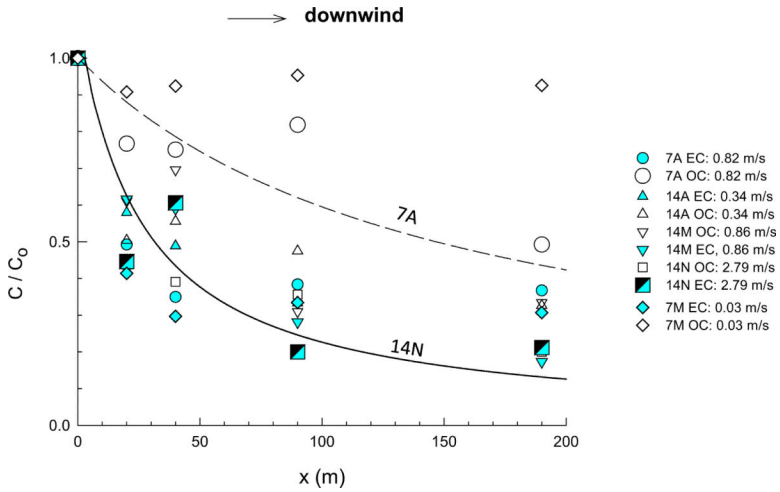

Fig. 8.

C/C_0 change in roadside dispersion in downwinds for OC (open) and EC (solid) under u_x various values. Regression lines are based on Eq. (5).

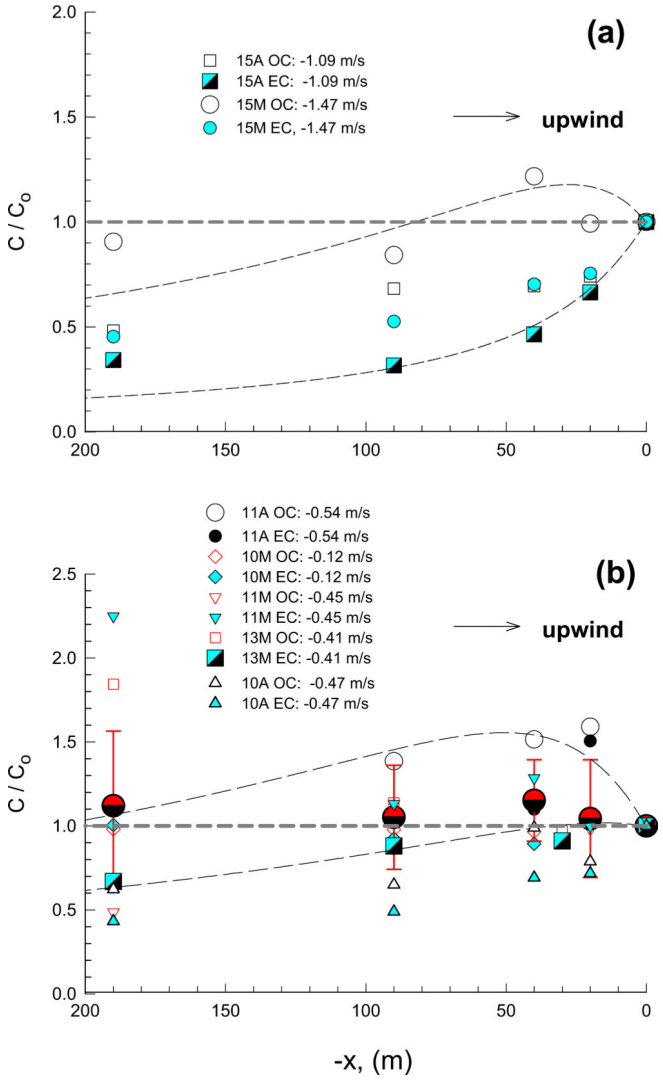

Fig. 9.

C/C_0 change in roadside dispersion in A) high upwinds; and B) oblique low winds for OC (open) and EC (solid) under various u_x values. Solid circle with error bar indicate geomean and 1σ. Regression lines are based on Eq. (5).

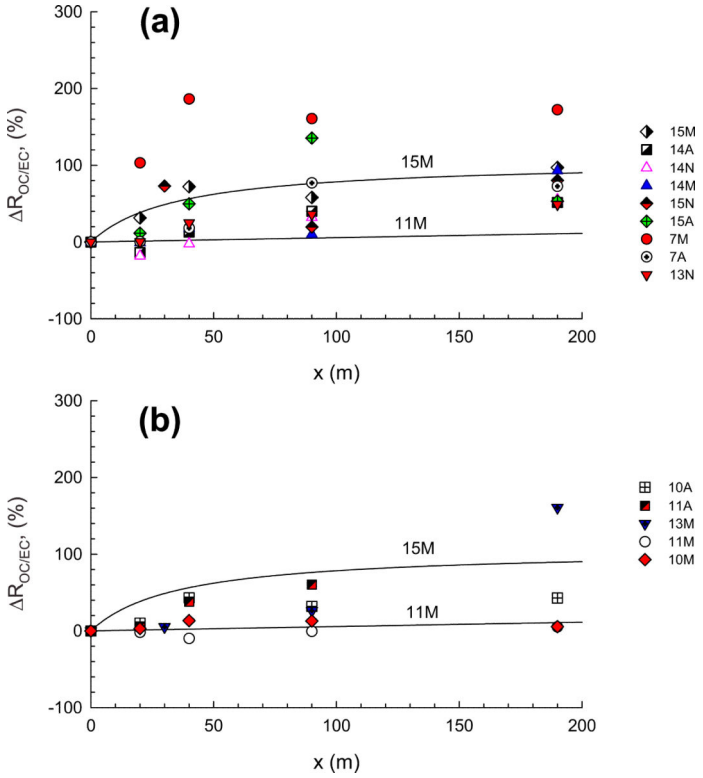

Fig. 10.

R% change of OC and EC in PM2.5 in roadside transport for the two groups: A) Gaussian dispersion; b) uniform distribution. 15M and 11M lines are based on Eq. (6).

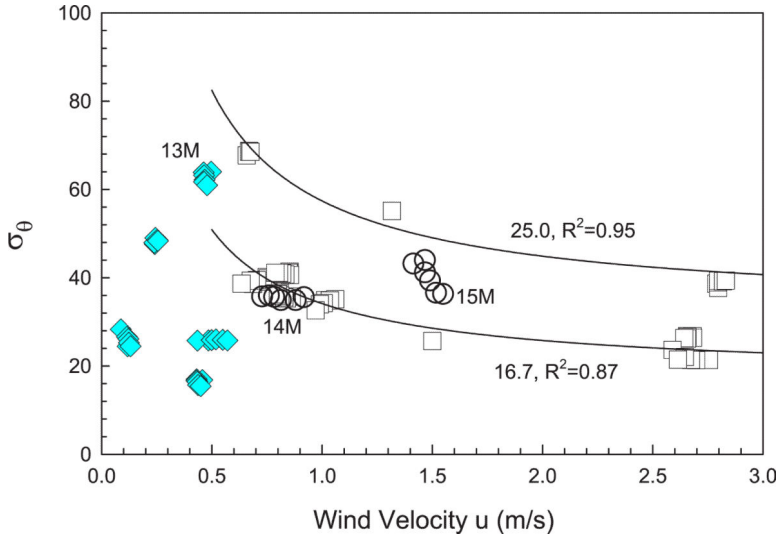

Fig. 11.

Correlations between u and σ_θ for the morning (filled diamond, open circle) and noon–afternoon (open square) periods. Two model lines in $\sigma_\theta \sim 1/u$ (Hanna, 1983) mark the wind field envelop of the noon–afternoon variations due to atmospheric turbulence. σ_θ is the standard deviation of wind angle θ.

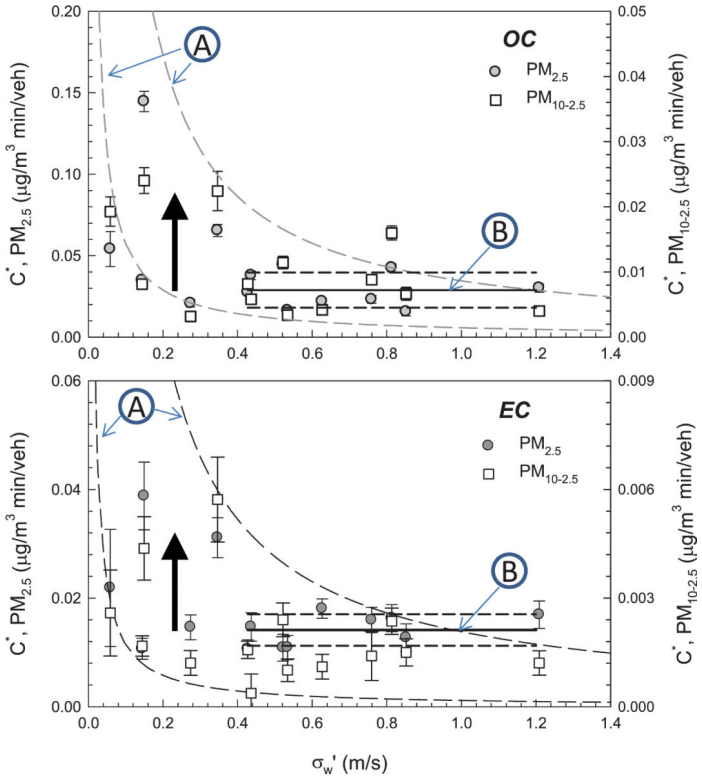

Fig. 12.

Variations with σ_w', the overall wind velocity variance, for OC and EC in $PM_{2.5}$ and $PM_{10–2.5}$. Model lines: A) $C^* \sim 1/\sigma_w'$ of Venkatram et al. (2007); B) $C^* \sim p(\theta)$ line (m ± 1σ). Arrows indicate possible meandering effect.

Table 1

Meteorological and traffic conditions.

Sampling event		Time	Wind condition				T (°C)[a]	ρ_{air} (mg m^{-3})[a]	Traffic flow (veh min^{-1})[c]			
			Calm, %	u (m s^{-1})[a,b]	θ(°)[a]	$u \sin \theta$			PC	TK	Total	TK%
Thur	7M	7:14–9:22	80.2%	0.12 (0.29)	17 (24.5)	0.034	13.50 (1.2)	1.228 (0.011)	153	14	167	8.4%
	7A	16:21–19:45	13.0%	0.82 (0.94)	87 (41.2)	0.819	25.60 (1.1)	1.173 (0.014)	144	11	156	7.1%
Sun	10M	7:09–10:07	29.9%	0.51 (0.58)	–166.2 (25.8)	–0.122	14.20 (1.9)	1.219 (0.011)	60	3	63	4.8%
	10A	16:28–19:22	5.8%	0.81 (0.83)	–144.6 (35.9)	–0.469	30.50 (0.9)	1.140 (0.013)	137	5	142	3.5%
Mon	11M	7:18–9:54	9.9%	0.46 (0.37)	–77.3 (16.8)	–0.449	15.79 (1.13)	1.205 (0.008)	128	14	142	9.9%
	11A	16:34–19:09	7.0%	0.81 (0.68)	–41.5 (40.4)	–0.537	29.60 (1.01)	1.146 (0.010)	146	11	157	7.0%
Wed	13M	7:20–10:11	0.28	0.50 (0.51)	–55.0 (64.0)	–0.410	14.22 (1.04)	1.220 (0.008)	131	16	147	10.9%
	13N	11:22–15:21	8.4%	0.66 (0.58)	–15.5 (67.7)	–0.176	23.31 (1.68)	1.159 (0.011)	130	20	149	13.4%
Thur	14M	7:09–9:54	6.0%	0.88 (0.87)	101 (34.9)	0.863	10.53 (0.70)	1.237 (0.006)	154	14	168	8.3%
	14N	11:40–15:02	0.0%	2.79 (1.20)	90 (38.7)	2.790	17.26 (1.04)	1.199 (0.006)	124	21	145	14.5%
	14A	16:39–19:43	4.1%	1.01 (0.80)	160 (34.9)	0.340	18.56 (0.81)	1.197 (0.007)	147	12	159	7.5%
Fri	15M	7:03–9:32	0.0%	1.47 (0.88)	–95.2 (44.0)	–1.464	11.96 (0.28)	1.227 (0.002)	143	14	157	8.9%
	15N	11:33–15:18	0.0%	2.66 (1.05)	–36.0 (27.0)	–1.564	16.79 (0.73)	1.195 (0.004)	120	18	138	13.0%
	15A	16:24–19:09	0.0%	2.59 (1.29)	–29.7 (23.7)	–1.283	17.94 (0.33)	1.200 (0.004)	158	10	168	6.0%

[a] All measurements in (m ± σ).

[b] Average wind speed including calm winds.

[c] Average traffic flow for sampling period.

Table 2

Observed black carbon variability and concentration range at road (M_1) and in the near-road stations.

Controlling factor	Period	Wind condition				Statistics	Black carbon concentration (μg(m^3 min)^1 (veh)^1)			
		Wind	$u \sin(\theta)$(ms^{-1})	θ	sgu		$PM_{2.5}$		$PM_{10-2.5}$	
							OC	EC	OC	EC
Oblique low upwinds at road	Morning	Upwinds	(0, −0.5)	−117° to −175°	<0.4	Range[a]	0.128	0.028	0.021	0.005
						Maximum	0.145	0.039	0.024	0.006
						Average	0.050	0.018	0.012	0.002
Temperature at road	Noon-afternoon	All	>0.5, or <−0.5	Any	>0.4	Range[b]	0.028	0.007	0.013	0.002
						Average	0.031	0.014	0.007	0.001
Horizontal dispersion to roadside	All	All	>0.5, or <−0.5	Any	>0.4	Range[c]	0.018	0.009	0.005	0.001
						Average	0.015	0.010	0.005	0.001

[a] $C_{max} - C_{min}$ at M_1 in Fig. 6.

[b] $C_{max} - C_{min}$ at M_1 in Fig. 7.

[c] $C_{max} - C_{min}$ among M_1–M_5 in each roadside dispersion.